Hippocampus

Quantitative differences in the convergence of local pyramidal cells onto axo-axonic and basket cells in the hippocampal CA3 subfield

Journal:	*Hippocampus*
Manuscript ID:	Draft
Wiley - Manuscript type:	Research Article
Keywords:	intreneuron, EPSC, EPSP, dendritic arbor, in vitro

Section: Neurophysiology

Section Editor: Prof. Christopher McBain

Quantitative differences in the convergence of local pyramidal cells onto axo-axonic and basket cells in the hippocampal CA3 subfield

Orsolya I. Papp, Mária R. Karlócai, Irén E. Tóth, Tamás F. Freund and Norbert Hájos

Department of Cellular- and Network Neurobiology, Institute of Experimental Medicine, Hungarian Academy of Sciences, Budapest, Hungary

Abbreviated title: Excitatory inputs onto parvalbumin-positive interneurons in CA3

Number of Pages: 23
Number of Figures: 8
Number of Tables: 3

Corresponding author:

Norbert Hájos, PhD
Institute of Experimental Medicine
Hungarian Academy of Sciences
Szigony u. 43, Budapest, Hungary, H-1083
Phone: +36-1-210-9400/387
Fax: +36-1-210-9412
E-mail: hajos@koki.hu

Grant sponsor: National Office for Research and Technology
Grant number: OMFB-01678/2009
Grant sponsor: Hungarian Scientific Research Fund
Grant number: NNF 85659, K 83251
Grant sponsor: European Research Council

Keywords: interneuron, EPSC, EPSP, dendritic arbor, in vitro

Abstract

In the hippocampus, parvalbumin-expressing axo-axonic (AAC) and basket cells (BC) show different discharge patterns during distinct network states, but the cellular mechanisms underlying these differences are not well understood. Using whole-cell patch-clamp techniques, we investigated the single-cell properties and excitatory synaptic features of anatomically identified AACs and BCs in the CA3 region of mouse hippocampal slices. The results showed that BCs had lower threshold for action potential (AP) generation and lower input resistance, narrower AP and afterhyperpolarization than AACs. In addition, BCs fired with higher frequencies and with more modest accommodation compared to AACs. The kinetic properties of excitatory postsynaptic currents (EPSC), the rectification of AMPA receptor-mediated currents, the fraction of the NMDA receptor-mediated component in EPSCs, and the EPSC magnitude necessary to evoke an AP were similar in both cell types. However, smaller excitatory postsynaptic potential and lower intensity fiber stimulation in stratum oriens was necessary to drive firing in BCs. Moreover, the rate of spontaneous EPSCs in BCs was higher than in AACs. Neurolucida analysis revealed that the dendrites of BCs in strata radiatum and oriens were longer and more extensively ramified. Since the density of the excitatory synapses was estimated to be comparable in both cell types, we conclude that the more elaborated dendritic arbor of BCs ensures that they receive a larger number of proximal excitatory inputs. Thus, CA3 pyramidal cells more profoundly innervate BCs than AACs, which could explain, at least in part, their distinct spiking behavior under different hippocampal network activities.

Introduction

In cortical structures, the mode of excitatory neuronal firing and the relationship of their spikes to synchronous network activities is a hallmark of differences in information processing. Since action potential generation in excitatory neurons is thought to be substantially regulated by diverse types of GABAergic cells innervating their perisomatic region (Miles et al., 1996, Freund and Katona, 2007), more precise control of neuronal function can be achieved if these interneurons spike differentially during different brain states. Indeed, interneurons synapsing on perisomatic membranes and expressing the Ca^{2+} binding protein parvalbumin (PV), such as basket cells (BC) or axo-axonic cells (AAC), spike in a distinguishable manner in somatosensory cortex upon whisker stimulation (Zhu and Zhu, 2004), in the basolateral amygdala (Bienvenu et al., 2012) and in the prefrontal cortex (Massi et al., 2012) upon a painful stimulus, or during hippocampal network oscillations (Klausberger et al., 2003). However, the cellular mechanisms underlying the different spiking behavior of these PV-immunopositive (PV+) interneurons during distinct neuronal operations are largely unknown.

PV+ interneurons in cortical areas provide a rapid feed-forward and feed-back control of pyramidal cell activities (Pouille and Scanziani, 2001, Freund and Katona, 2007, Cruikshank et al., 2010). This fast recruitment of inhibition is ensured partly by their unique input properties. In the hippocampus, excitatory postsynaptic potentials (EPSPs) received by these interneurons have a short latency and rapid kinetics (Miles, 1990). This is in part due to fast synaptic currents mediated by AMPA receptors containing the GluA4 subunit (Jonas et al., 1994, Geiger et al., 1995), to the fast clearance of glutamate from the synaptic cleft (Geiger et al., 1997), and to the distinctive electrical properties of PV+ interneuron dendrites (Hu et al., 2010, Nörenberg et al., 2010). Since these GABAergic cells receive relatively large excitatory inputs from each of their presynaptic pyramidal cells, which can even drive AP generation (Gulyás et al., 1993b, Ali et al., 1998, Woodruff et al., 2011), PV+ interneurons can readily monitor the activity of excitatory cell assemblies (Galarreta and Hestrin, 2001). These features together provide PV+ interneurons with a narrow time window for synaptic integration, ensuring fast and precisely timed spike generation (Glickfeld and Scanziani, 2006), a pivotal feature for oscillogenesis at different frequencies (Freund and Katona, 2007, Fuchs et al., 2007, Sohal et al., 2009). However, in these previous studies, AACs were not separated from BCs, and so the differential synaptic recruitment of these

PV+ interneurons that might potentially underlie their distinct network behavior has remained elusive.

We used a combined *in vitro* electrophysiological and anatomical approach to investigate the properties of excitatory synaptic transmission, the spiking characteristics and the excitability of AACs and BCs in the CA3 region of the hippocampus. We found rather similar properties in the excitatory synaptic inputs of these interneurons, but significant differences in their membrane features. In addition, a more extensive arborization in the proximal dendrites of BCs was observed compared to AACs, which may ensure that a larger number of CA3 pyramidal cells can excite BCs in this hippocampal region.

Materials and Methods

Animals and Slice Preparation. Experiments were approved by the Committee for the Scientific Ethics of Animal Research (22.1/4027/003/2009) and were performed according to the guidelines of the institutional ethical code and the Hungarian Act of Animal Care and Experimentation (1998. XXVIII. section 243/1998.). Transgenic mice expressing enhanced green fluorescent protein (EGFP) under the control of the PV promoter were used (Meyer et al., 2002).

Mice aged between P15 and P23 were deeply anaesthetized with isoflurane and decapitated. The brain was quickly removed from the skull and immersed into ice-cold solution containing (in mM): sucrose 252; KCl 2.5; $NaHCO_3$ 26; $CaCl_2$ 0.5; $MgCl_2$ 5; NaH_2PO_4 1.25; glucose 10; bubbled with 95% O_2 / 5% CO_2 (carbogen gas). Horizontal hippocampal slices of 150-200 µm thickness were cut using a Leica VT1000S or VT1200S Vibratome (Wetzlar, Germany), and placed into an interface-type holding chamber containing artificial cerebrospinal fluid (aCSF) consisting of (in mM): NaCl, 126; KCl, 2.5; $NaHCO_3$, 26; $CaCl_2$, 2; $MgCl_2$, 2; NaH_2PO_4 1.25; glucose 10 at 36 ºC that gradually cooled down to room temperature (~1-1.5 hours). After incubation (at least an hour), slices were transferred individually into a submerged type recording chamber.

Electrophysiological recordings. Loose-patch and whole-cell patch-clamp recordings were performed under visual guidance using a Nikon FN1 microscope equipped with differential interference contrast optics. EGFP in cells were excited by a UV lamp, and the fluorescence was visualized by a CCD camera (C-7500; Hamamatsu Photonics, Japan). Patch pipettes were pulled

from borosilicate glass capillaries with an inner filament (1.5 mm O.D.; 1.12 mm I.D., Hilgenberg, Germany) using a DMZ-Universal Puller (Zeitz-Instrumente GmbH, Germany). For loose-patch recordings, glass pipettes (~3-5 MΩ) were filled with aCSF, for whole-cell recordings the intracellular solution contained (in mM): K-gluconate 110; NaCl 4; HEPES 20; EGTA 0.1; phosphocreatine-di-(tris) salt 10; Mg-ATP 2; Na-GTP 0.3; spermine 0.1; and 0.2 % biocytin (pH 7.3 adjusted with KOH; osmolarity 290 mOsm/l). To obtain a current-voltage (tom Dieck et al.) relationship for excitatory postsynaptic currents (EPSC), an intracellular solution containing (in mM): CsCl 80; Cs-gluconate 60; $MgCl_2 \times 6H_2O$ 1; Mg-ATP 2; HEPES 10; NaCl 3; QX-314Cl 5; spermine 0.1; and 0.2 % biocytin (pH 7.3 adjusted with KOH; osmolarity 290 mOsm/l) was used. Data were recorded with a Multiclamp 700B amplifier (Axon Instruments, Foster City, CA, USA), low-pass filtered at 2 kHz and digitized at 10 kHz with a PCI-6024E A/D board (National Instruments, Austin, TX, USA) using EVAN 1.3 (courtesy of Professor Istvan Mody, Departments of Neurology and Physiology, UCLA, CA) or in Stimulog software (courtesy of Prof. Zoltán Nusser, Institute of Experimental Medicine, Hungarian Academy of Sciences, Budapest, Hungary). Recordings were analyzed with EVAN 1.3 and with an in-house analysis software SPIN 1.0.1 (courtesy of Prof. Zoltán Nusser).

Slices were superfused with aCSF containing 5 µM SR 95531 (gabazine) to block $GABA_A$ receptor-mediated conductance. The flow rate was adjusted to 3 ml/min. Recordings were obtained at 30-32 °C. Spontaneous EPSCs (sEPSC) were measured at -60 mV. Excitatory postsynaptic potentials (EPSPs) and currents (EPSCs) evoked by gradually increasing stimulus intensities near the firing threshold of the cells were recorded at the resting membrane potential (RMP) of the cells, which was measured immediately after break-in. At each stimulus intensity, six EPSPs or EPSCs were recorded. Electrical stimulation of fibers was delivered via a Pt-Ir bipolar electrode (tip diameter of 10-20 µm, Neuronelektród Kft., Budapest, Hungary) every 10 s (0.1 Hz) using a Supertech timer and isolator (Supertech Ltd., Pécs, Hungary). The stimulating electrode was placed into the stratum oriens in the CA3 region in order to stimulate the CA3 recurrent collaterals but avoid mossy fibers derived from granule cells located mainly in the stratum lucidum. The stimulation site was within 100 µm of the recorded cells. Access resistance (between 5-15 MΩ) was frequently monitored and recordings with a change in access resistance >20% were excluded from the analysis. Recordings were not corrected for junction potential. Before recording of synaptic currents, we tested the voltage response to a series of

hyperpolarizing and depolarizing square current pulses of 800 ms duration and amplitudes between -100 and 100 pA at 10 pA step intervals, then up to 300 pA at 50 pA step intervals and finally up to 600 pA at 100 pA step intervals from a holding potential of -60 mV in each cell. Using these voltage responses, we characterized active and passive membrane properties of AACs and BCs (for details, see (Antal et al., 2006, Zemankovics et al., 2010). Rheobase was defined as the current step required to fire at least 3 action potentials. The maximal current step was the highest current injection generating firing with lack of distortion.

To characterize the current-voltage relationship, we recorded electrically evoked EPSCs (eEPSCs) at different holding potentials (at -60, -40, -20, +20 and +40 mV) under control conditions and in the presence of 10 μM NBQX, which is an antagonist of non-NMDA types of ionotropic glutamate receptors. AMPA/KA receptor-mediated currents were calculated by subtraction of responses measured in the presence of NBQX from control responses. Rectification index was taken as the ratio of AMPA/KA receptor-mediated conductances at -60 mV and +40 mV. The fraction of NMDA receptor-mediated current to all ionotropic receptor-mediated currents was calculated by dividing NMDA receptor-mediated conductances in the presence of NBQX with the size of control EPSCs measured at -40 mV.

Separation of axo-axonic cells and basket cells. After recordings, hippocampal slices were fixed overnight in 4% paraformaldehyde in 0.1 M PB, pH 7.4. Following fixation, slices were washed with 0.1 M PB several times. Biocytin-filled cells were visualized with Alexa 488- or Alexa 594-conjugated strepavidin (Alexa 488, 1:3000; Alexa 594, 1:1000; Invitrogen, Carlsbad, CA, USA). At this stage, we made high resolution 3D images from the cells in z-stack mode with 1-2 μm steps using a FV 1000 Olympus confocal microscope (20x Objective, N.A.=0.75) to reconstruct the dendritic trees with Neurolucida software.

To distinguish between axo-axonic cells (AAC) and basket cells (BC), the close proximity of biocytin-labeled axon endings with axon initial segments was inspected (see Gulyás et al., 2010). Axon initial segments were visualized by an immunostaining against the protein Ankyrin G. Slices were embedded in 1% agar and re-sectioned to 40 μm thickness. The sections were then treated with 0.1 mg/ml pepsin (Cat. No. S3002; Dako, Glostrup, Denmark) in 1 N HCl at 37 °C for 15 min and were washed in 0.1 M PB. Sections were blocked in normal goat serum (NGS, 10%, Vector Laboratories, Burlingame, CA) made up in Tris-buffered saline (TBS, pH 7.4)

followed by incubation in mouse anti-AnkyrinG (Santa Cruz Biotechnology, Santa Cruz, CA) diluted 1:100 in TBS containing 2% NGS and 0.05% Triton X-100. Following several washes in TBS, Alexa 594-conjugated goat anti-mouse (1:500) or Alexa 488-conjugated goat anti-mouse (1:500) was used to visualize the axon initial segments, depending on the color of biocytin labeling. Maximum intensity *z*-projection images of 4 confocal stacks were taken using an A1R confocal laser scanning microscope using a 60× (NA = 1.4) objective (Nikon Europe, Amsterdam, The Netherlands).

Estimating the density of VGluT1-expressing synapses onto biocytin-labeled dendrites. *A*fter re-sectioning the slices to 40 µm thickness, sections were blocked in 5% NGS and 5% normal horse serum made up in Tris-buffered saline (TBS), pH 7.4, followed by incubation in guinea-pig anti-VGluT1 (1:10,000, Millipore, Billerica, MA) and mouse anti-Bassoon (1:3000, Abcam, Cambridge, UK) antibodies diluted in TBS containing 0.5% Triton X-100. Following several washes in TBS, the sections where biocytin was developed with Alexa 594-conjugated streptavidin were treated with a mixture of Alexa 488-conjugated donkey anti-mouse and DyLight 405-conjugated donkey anti-guinea pig antibodies (1:500; Jackson ImmunoResearch, Bar Harbor, MA). If biocytin was visualized with Alexa 488-conjugated streptavidin, a mixture of Cy3-conjugated goat anti-mouse (1:500; Invitrogen, Carlsbad, CA) and DyLight 405-conjugated donkey anti-guinea pig antibodies was applied to the sections. After several washes, sections were mounted on slides in Vectashield (Vector Laboratories). Images were taken using an A1R confocal laser scanning microscope (Nikon Europe, Amsterdam, The Netherlands) using a 60× (NA = 1.4) objective. For high magnification images, single confocal images or maximum intensity *z*-projection images were used (2-3 confocal images at 0.3-3 µm). From 4 AACs, 9 dendritic segments in the stratum oriens, 10 in the strata pyramidale and lucidum and 11 in the stratum radiatum were imaged and investigated. From 4 BCs, six dendritic segments were sampled in each layer and analyzed. To improve the quality of the images, deconvolution was carried out with the Huygens Professional program (Hilversum, The Netherlands).

After deconvolution, the number of VGluT1-immunostained boutons forming close appositions with the biocytin-labeled dendrites, where Bassoon staining within the boutons was unequivocally present facing toward the dendrite, were counted using the NIS-viewer software (Nikon Europe). Dendritic surface was calculated by measuring the length, depth and radius of

the dendrites with the aid of the NIH ImageJ image analyser software. Bassoon- or VGluT1-positive single stained elements were not counted. After calculating the surface of the dendritic segment, the Bassoon- and VGluT1-double-immunopositive inputs were quantified and normalized to 50 μm^2. Similar results were obtained with the two different mixtures of antibodies, and therefore the data were pooled.

Neurolucida analysis. Dendrites of recorded cells were reconstructed with Neurolucida 5.0 software using the 3D confocal images taken before re-sectioning. Values were corrected for shrinkage of tissue. Branched Structure, Convex Hull and Sholl Analyses were performed on the reconstructed dendrites. For Sholl analysis, concentric spheres at 50 µm radius intervals were drawn around the cell, centered on the cell body, and several dendritic parameters were measured independently for each shell. To correlate sEPSC rate with dendritic length for each cell, the dendritic length at different distances from the soma was calculated as the sum of data in shells obtained in Sholl analysis until the given sphere border.

.

Statistical analysis. In all cases, the non-parametric Mann-Whitney test was applied, using STATISTICA 11 software (Statsoft, Inc., Tulsa, OK) or Origin 8.6 software (Northampton, MA). Data are presented as median and interquartile range. Before correlation tests for linear values, the normality of a distribution was tested by the Shapiro-Wilk and Kolmogorov-Smirnov tests. As the tests did not reject normality ($p>0.05$), the Pearson's correlation coefficient was used.

Drugs. All chemicals and drugs were purchased from Sigma Aldrich (St Louis, MO, USA), except gabazine (SR95531) and spermine, which were obtained from Tocris (Bristol, UK).

Results

Identification of parvalbumin-positive axo-axonic and basket cells using Ankyrin-G immunostaining

To investigate the properties of PV+ interneurons in the CA3 region of the hippocampal slices, we used a mouse line expressing eGFP under the control of the PV promoter (Meyer et al., 2002). After whole-cell recordings, the slices were fixed and the biocytin content of interneurons was revealed, allowing *post hoc* anatomical identification of the recorded cells. Only cells possessing an axon arbor predominantly in stratum pyramidale were included in this study (n=87). Basket cells (BC) targeted mainly stratum pyramidale, but their axon collaterals could be traced to the proximal strata oriens, lucidum, and radiatum (n=28). In the case of axo-axonic cells (AAC, n=59), the axon arbor was shifted towards the border of strata pyramidale and oriens, where most pyramidal cells axon initial segments (AIS) are located (Figure 1A, B). To unequivocally distinguish AACs and BCs, we performed double immunolabeling for biocytin and Ankyrin-G in all cases. Ankyrin-G is an anchoring protein (Jenkins and Bennett, 2001) accumulating predominantly in the AIS (Boiko et al., 2007). Interneurons were identified as AACs if the axon terminals of labeled cells formed close appositions with AISs, or as BCs if their axons avoided the Ankyrin-G immunoreactive elements (Figure 1A, B).

Membrane properties of AACs and BCs in the hippocampal CA3 region

From the voltage responses upon the injection of a series of hyperpolarizing and depolarizing square current pulses into the interneurons, we first determined their active and passive membrane properties (Figure 1C-E, Table 1). We found that the rheobase of BCs was significantly higher, whereas their AP threshold was lower, than that of AACs in response to rheobase current steps. The afterhyperpolarization (AHP) shape of BCs was narrower, as indicated by significantly lower AHP widths at 25, 50 and 75% of the amplitude. In contrast, we found no differences in the AHP amplitude. At maximal current injection, the half width of action potentials in BCs was significantly shorter, and these cells displayed significantly higher AP

frequency with lower accommodation than AACs. Adaptation in the amplitude of APs was not different between cell types. The resting membrane potential obtained immediately after break-in into AACs and BCs was found to be comparable. The membrane time constant, capacitance and relative sag amplitude of the two cell types were also similar, but BCs had a significantly lower input resistance (Table 1).

As AACs had a higher AP threshold than BCs in response to near-threshold current steps, we sought to find a possible difference in the structural organization of the AIS. We examined the length of the Ankyrin-G-immunopositive segment and the distance of its beginning from the soma, since previous studies have shown that these features could correlate with the variability in AP threshold (Grubb and Burrone, 2010, Kuba et al., 2010). The investigation revealed that the length of the Ankyrin-G-immunopositive segment in the AISs and the distance of its beginning from the soma were not different between AACs and BCs, suggesting that these structural properties of the AIS are not responsible for the difference observed in the AP threshold (Table 3).

BCs receive a higher number of proximal excitatory synaptic inputs than AACs

Next, we aimed to establish the magnitude of excitatory synaptic inputs necessary to evoke an AP in AACs and BCs. To this end, we stimulated CA3 recurrent collaterals in the stratum oriens with gradually increasing stimulus intensities and recorded first in loose-patch mode, followed by measurements obtained in current-clamp and voltage-clamp mode (Figure 2A, B). The stimulus intensity necessary to induce spiking in cells using extra- or intracellular recordings showed a strong correlation (minimal stimulus intensity for AACs, r^2=0.977, p<0.001, n=7; for BCs, r^2=0.8, p=0.004, n=7; maximal stimulus intensity for AACs: r^2=0.682, p=0.013, n=7; for BCs, r^2=0.965, p<0.001, n=6; Figure 2C), suggesting that whole-cell recordings did not significantly perturb spiking properties or excitatory synaptic transmission. This allowed us to determine the EPSP and EPSC amplitude at AP threshold. Thus, by measuring the size of synaptic inputs in whole-cell mode at those stimulus intensities that were needed to evoke AP firing, we could compare the properties of excitatory synaptic inputs at spiking threshold in AACs and BCs (Figure 2D). We found that the magnitude of the electrically evoked EPSPs (eEPSPs) necessary to discharge the cell at the resting membrane potential was smaller in BCs

than in AACs (Figure 2E, Table 2). In contrast, the EPSC amplitudes evoked under the same conditions in both interneuron types were similar. Importantly, evoking APs in BCs required significantly lower stimulus intensities than in AACs (Figure 2F), but the maximal values for EPSPs and EPSCs, which could be triggered by focal stimulation, were comparable (Table 2). These data suggest that there are some differences in the excitatory synaptic inputs to these two types of PV+ interneurons.

In the next set of experiments, our goal was to clarify the kinetics of evoked EPSCs (eEPSCs) and the properties of AMPA and NMDA receptor-mediated synaptic currents in PV+ interneurons. Our analysis revealed that the 20-80 % rise time and decay time constant of EPSCs evoked in AACs and BCs at the membrane potential of -60 mV was similar (Figure 3, Table 2). In addition, we obtained the I-V curves for AMPA receptor-mediated synaptic currents by measuring the EPSC amplitudes in the absence and presence of NBQX (5 μM; Figure 4A), and subtracting the NMDA receptor-mediated component from the averaged traces obtained under drug-free conditions. In both interneuron types, the AMPA receptor-mediated synaptic currents showed strong inward rectification in a similar manner (Figure 4B, Table 2), indicating that AMPA receptors with high Ca^{2+} permeability should mediate fast EPSCs (Geiger et al., 1995). Furthermore, we also compared the proportion of NMDA receptor-mediated currents in the evoked synaptic responses and found no difference between the two cell types (Figure 4B, Table 2). These results propose that EPSCs in AACs and BCs are mediated via ionotropic glutamate receptors with similar properties.

To further examine the features of excitatory synaptic inputs received by PV+ cells, we recorded spontaneously occurring EPSCs (sEPSCs) in AACs and BCs (Figure 5A). In agreement with our eEPSC parameter data, the peak amplitude, 20-80% rise time and decay time constant of sEPSC were comparable in both interneuron types (Figure 5B, Table 2). In contrast, the interevent interval of sEPSCs measured in BCs was significantly lower, and thus the sEPSC rate was higher, compared to that recorded in AACs (Figure 5B, Table 2). These observations indicate a higher number of excitatory synaptic inputs in BCs compared to AACs.

The density of excitatory synapses on the proximal dendrites of AACs and BCs is similar

The higher sEPSC rate and the lower stimulus intensity required for AP generation by focal stimulation in BCs propose that the number of excitatory synaptic inputs received by the proximal parts of BCs might be higher compared to AACs. This difference can be due to the fact that the dendrites of BCs might be covered with excitatory synapses more densely, but the length of proximal dendrites for both cell types is similar. Alternatively, the density of excitatory synaptic inputs can be similar for both cell types, but the proximal dendrites of BCs may be longer or more numerous than of AACs. To distinguish between these two possibilities, we estimated the density of excitatory synapses received by the dendrites of both cell types. We calculated the number of VGluT1- and Bassoon-double-immunopositive axon endings forming close appositions with the biocytin-labeled dendrites of PV+ cells. VGluT1 is a marker for cortical excitatory synapses (Kaneko and Fujiyama, 2002, Fremeau et al., 2004), while Bassoon is present at the presynaptic active zone (tom Dieck et al., 1998, Richter et al., 1999), allowing us to determine whether synapses in the axon endings are indeed closely apposed to the biocytin-filled dendrites or face unlabelled profiles (Figure 6A-F). We randomly sampled biocytin-positive dendritic segments in three different layers (stratum oriens, proximal region -including strata pyramidale and lucidum- and stratum radiatum) and found a similar number of excitatory axon endings apposed to both cell types (Figure 6G, Table 3). In conclusion, our data show that the density of VGluT1-immunopositive axon endings on the proximal dendrites of both AACs and BCs is similar.

BCs have significantly longer dendrites with a more extensive proximal arborization compared to AACs

Since we have not observed any difference in the density of excitatory synapses received by the dendrites of the two interneuron types, we next investigated the structure of the dendritic trees of AACs and BCs to clarify the possible reasons underlying the difference in sEPSC rate and the stimulus intensities needed to discharge them (Table 3). We reconstructed the dendritic arbor of biocytin-filled cells with the Neurolucida software using the 3D confocal images taken from the recorded neurons (Figure 7A). We measured several dendritic parameters including total dendritic length, dendritic length in each hippocampal layer (Figure 7B) or as a function of dendritic order, number of dendrites, number of nodes (Figure 7C), soma surface, and the highest

order dendritic segment with Branched Structure Analysis. The volume occupied by the cells was measured with Convex Hull Analysis and the number of apical and basal intersections as a function of distance from the soma was analyzed using Sholl Analysis (Figure 7D). We found that the soma surface of AACs and BCs was similar (Figure 7B). In contrast, the dendrites of BCs were longer by 50% compared to that observed for AACs, which was due to significantly longer dendrites in strata oriens and radiatum (Table 3). In addition, the 3rd and 5th order dendrites of BCs were longer and more numerous, while their 2nd and 4th order dendrites had more nodes than AACs (Figure 7C). These observations are in accordance with the Sholl Analysis, which also revealed a higher number of dendrite:shell intersections in BC proximal regions, both in the strata radiatum and oriens. Median values of apical and basal intersections for the two PV+ cell types indicated that in BCs, both the apical and basal parts of the dendrites exhibited more extensive arborization closer to the cell body. In contrast, the distal dendrites of AACs in the apical part, closer to or within the stratum lacunosum-moleculare ramified more intensely than that of BCs. This was supported by the significantly higher ratio of distal versus proximal intersections in AACs (i.e. at 300/150, 350/150, 300/200, 350/200 µm; Table 3). We found no difference in the highest order of dendritic segments, indicating that the total branching number is similar, but the structure of branching is different. Consistently, Convex Hull Analysis showed that the occupied volume of the two cell types is equal. Thus, BCs tend to be more ramified and more symmetric, while AACs are more polarized with a characteristic tuft in the apical part of their dendrites. This structural difference observed for BCs, especially the longer dendrites and denser proximal arborization could explain the higher rate in sEPSC occurrence and the lower stimulus intensities necessary to evoke APs in them by focal stimulation of fibers in the stratum oriens.

If this assumption is valid, then the number and/or length of proximal dendrites should correlate with the rate of sEPSCs. Indeed, we found a strong link between the sEPSC rate and the dendritic length at distances of 50 and 100 µm from the soma (at 50 µm, r=0.82, p=0.014; at 100 µm, r=0.75, p=0.03; Figure 8A, B). Up to 300 µm, the correlation was less strong (at 150 µm, r=0.68, p=0.061; Figure 8C, at 200 µm, r=0.66, p=0.075; at 250 µm, r=0.67, p=0.067), but was also significant at 300 µm (r=0.73, p=0.039). At 350 µm from the soma, there was no correlation between dendritic length and sEPSC rate (r=0.54, p=0.169; Figure 8D). These results strengthen the idea that the larger number of excitatory synaptic inputs received by BCs is due to their longer dendritic tree.

Discussion

In this study we have investigated the single-cell properties, excitatory synaptic input features and the morphological characteristics of AACs and BCs in the CA3 region of the hippocampus. We found that, in comparison to AACs, BCs have a lower AP threshold and input resistance, a narrower AP and AHP, and a higher spike frequency with no accommodation. EPSC properties in both cell types were comparable, except we recorded a higher rate of sEPSCs in BCs. The stimulus intensity needed to evoke spiking in BCs was lower, although the EPSC magnitude necessary for AP generation was similar in both interneuron types. In addition, we revealed that the density of excitatory synapses at proximal dendrites was similar in both PV+ cell types, but BCs have significantly longer dendrites, which ramify more extensively in the strata oriens and radiatum compared to AACs. These structural differences might explain, at least in part, the observed differences in sEPSC rate and lower stimulus intensity necessary to evoke EPSCs at AP threshold in BCs by stimulating recurrent collaterals in the stratum oriens.

Single-cell properties of PV+ interneurons targeting the perisomatic region in cortical areas

In accord with previous findings in cortical structures (Buhl et al., 1994, Kawaguchi, 1995, Cauli et al., 1997, Kawaguchi and Kubota, 1997, Pawelzik et al., 2002), we observed that the perisomatic region-targeting PV+ interneurons have fast-spiking properties with moderate accommodation, low input resistance and narrow APs with large and fast AHPs compared to that characterized in other types of GABAergic cells (Freund and Buzsáki, 1996, Ascoli et al., 2008). These features in AACs and BCs, however, were found to be distinct both in CA3 and somatosensory cortex (present study, (Woodruff et al., 2009, Xu and Callaway, 2009), indicating that pooling data of comparable, but not identical, interneuron types can mask differences that might be important to understand the function of these interneurons in neuronal networks. We also observed that BCs exhibited significantly higher spike frequency and a lower accommodation ratio than AACs, implying a potential difference in Kv3 potassium conductance, which is pivotal for the fast-spiking phenotype (Lien and Jonas, 2003, Goldberg et al., 2011). The threshold for AP generation was higher in AACs than in BCs, although the Ankyrin-G staining in

AISs, which was shown to correlate with the location of voltage-gated Na+ channels (Jenkins and Bennett, 2001, Grubb and Burrone, 2010), was similar in both cell types. This observation suggests that the difference in AP threshold cannot be explained simply by a structural discrepancy in AIS organization, in contrast to that found in other cell types (Grubb and Burrone, 2010, Kuba et al., 2010). Interestingly, we found that the same EPSC amplitude was necessary to evoke an AP in both cell types, in spite of the fact that AACs had a higher AP threshold. A plausible explanation for this contradiction can be that AACs have a larger input resistance, giving rise to larger voltage change in these interneurons when equal synaptic current is evoked in BCs and AACs. Indeed, the magnitude of EPSPs near AP threshold was significantly larger in AACs than in BCs. Thus, the higher AP threshold and input resistance in AACs ensures that at similar resting membrane potential the same synaptic current is needed to discharge both PV+ interneuron types. Since in the thin slices used here sEPSCs correspond mostly to unitary events with a similar amplitude in both interneuron types (Table 2), and PV+ interneurons in CA3 are innervated mainly via single synaptic contacts (Sík et al., 1993), we conclude that the spiking of AACs and BCs in this hippocampal region should be driven to fire APs by a similar number of excitatory neurons.

Distinct innervation of AACs and BCs by glutamatergic afferents

The morphological analysis of the dendritic trees of intracellularly-labeled interneurons in CA3 showed that BCs had longer and more arborized dendrites in the strata oriens and radiatum than AACs. In contrast, the density of excitatory synapses received by the proximal dendrites of both interneuron types was estimated to be comparable. These data together could explain our electrophysiological observations, namely that a lower intensity of focal stimulation was necessary to evoke EPSCs with the similar amplitudes in BCs compared to AACs, and the sEPSC rate was higher in BCs than in AACs. The strong relationship found between the sEPSC rates recorded in individual interneurons and the length of their dendritic branches also strengthens this conclusion (Figure 8). Since CA3 pyramidal cells innervate PV+ interneurons mainly via single release sites localized predominantly in the strata oriens and radiatum (Gulyás et al., 1993b, Sík et al., 1993), our results suggest that more numerous excitatory neurons can excite BCs than AACs in this hippocampal region. Knowing that individual BCs inhibit a larger number of

pyramidal cells than AACs (Gulyás et al., 1993a), BCs and AACs should be embedded quite differently into intrahippocampal networks. Another difference in their excitatory afferentation is the proportion of the synaptic inputs with extrahippocampal origin. Comparable to that observed in CA1 (Li et al., 1992, Klausberger et al., 2003), we also found that the distal dendrites of AACs in CA3 have a tufted appearance, allowing them to receive a higher fraction of glutamatergic inputs from cortical or subcortical structures compared to BCs. Similarly to the cortex, AACs also have more polarized dendritic trees than BCs (Woodruff et al., 2011). These morphological data strongly argue for the distinct function of AACs and BCs in cortical operation (Dugladze et al., 2012).

Firing behavior of AACs and BCs during different network states.

AACs and BCs were found to discharge distinctly during characteristic network activities in the hippocampus. For instance, BCs fired more action potentials than AACs during gamma oscillations or sharp wave-ripple oscillations (Klausberger et al., 2003, Tukker et al., 2007, Gulyás et al., 2010), and they fired at different phases of the hippocampal theta rhythm. Additionally, recent studies have shown that the spiking response of AACs and BCs to a given external stimulus varies. In the basolateral amygdala (Bienvenu et al., 2012) or in the prefrontal cortex (Massi et al., 2012), AACs begin to fire at high frequency in response to painful stimuli, whereas BCs discharge at a rather lower rate. In the somatosensory cortex, in response to whisker stimulation, AACs were found to have a larger receptive field with a lower acuity compared to other fast-spiking neurons (Zhu and Zhu, 2004). Together these observations may propose that AACs can be more responsible for stimuli arriving from the external world, adjusting the significance of direct sensory inputs or their processed forms, while BCs could monitor and more faithfully control the activity of intracortical communication.

References

Ali AB, Deuchars J, Pawelzik H, Thomson AM (1998) CA1 pyramidal to basket and bistratified cell EPSPs: dual intracellular recordings in rat hippocampal slices. J Physiol 507 (Pt 1):201-217.

Antal M, Eyre M, Finklea B, Nusser Z (2006) External tufted cells in the main olfactory bulb form two distinct subpopulations. Eur J Neurosci 24:1124-1136.

Ascoli GA, Alonso-Nanclares L, Anderson SA, Barrionuevo G, Benavides-Piccione R, Burkhalter A, Buzsáki G, Cauli B, Defelipe J, Fairen A, Feldmeyer D, Fishell G, Fregnac Y, Freund TF, Gardner D, Gardner EP, Goldberg JH, Helmstaedter M, Hestrin S, Karube F, Kisvárday ZF, Lambolez B, Lewis DA, Marin O, Markram H, Munoz A, Packer A, Petersen CC, Rockland KS, Rossier J, Rudy B, Somogyi P, Staiger JF, Tamás G, Thomson AM, Toledo-Rodriguez M, Wang Y, West DC, Yuste R (2008) Petilla terminology: nomenclature of features of GABAergic interneurons of the cerebral cortex. Nat Rev Neurosci 9:557-568.

Bienvenu TC, Busti D, Magill PJ, Ferraguti F, Capogna M (2012) Cell-type-specific recruitment of amygdala interneurons to hippocampal theta rhythm and noxious stimuli in vivo. Neuron 74:1059-1074.

Boiko T, Vakulenko M, Ewers H, Yap CC, Norden C, Winckler B (2007) Ankyrin-dependent and -independent mechanisms orchestrate axonal compartmentalization of L1 family members neurofascin and L1/neuron-glia cell adhesion molecule. J Neurosci 27:590-603.

Buhl EH, Han ZS, Lőrinczi Z, Stezhka VV, Karnup SV, Somogyi P (1994) Physiological properties of anatomically identified axo-axonic cells in the rat hippocampus. J Neurophysiol 71:1289-1307.

Cauli B, Audinat E, Lambolez B, Angulo MC, Ropert N, Tsuzuki K, Hestrin S, Rossier J (1997) Molecular and physiological diversity of cortical nonpyramidal cells. J Neurosci 17:3894-3906.

Cruikshank SJ, Urabe H, Nurmikko AV, Connors BW (2010) Pathway-specific feedforward circuits between thalamus and neocortex revealed by selective optical stimulation of axons. Neuron 65:230-245.

Dugladze T, Schmitz D, Whittington MA, Vida I, Gloveli T (2012) Segregation of axonal and somatic activity during fast network oscillations. Science 336:1458-1461.

Fremeau RT, Jr., Kam K, Qureshi T, Johnson J, Copenhagen DR, Storm-Mathisen J, Chaudhry FA, Nicoll RA, Edwards RH (2004) Vesicular glutamate transporters 1 and 2 target to functionally distinct synaptic release sites. Science 304:1815-1819.

Freund TF, Buzsáki G (1996) Interneurons of the hippocampus. Hippocampus 6:347-470.

Freund TF, Katona I (2007) Perisomatic inhibition. Neuron 56:33-42.

Fuchs EC, Zivkovic AR, Cunningham MO, Middleton S, Lebeau FE, Bannerman DM, Rozov A, Whittington MA, Traub RD, Rawlins JN, Monyer H (2007) Recruitment of parvalbumin-positive interneurons determines hippocampal function and associated behavior. Neuron 53:591-604.

Galarreta M, Hestrin S (2001) Spike transmission and synchrony detection in networks of GABAergic interneurons. Science 292:2295-2299.

Geiger JR, Lübke J, Roth A, Frotscher M, Jonas P (1997) Submillisecond AMPA receptor-mediated signaling at a principal neuron-interneuron synapse. Neuron 18:1009-1023.

Geiger JR, Melcher T, Koh DS, Sakmann B, Seeburg PH, Jonas P, Monyer H (1995) Relative abundance of subunit mRNAs determines gating and Ca2+ permeability of AMPA receptors in principal neurons and interneurons in rat CNS. Neuron 15:193-204.

Glickfeld LL, Scanziani M (2006) Distinct timing in the activity of cannabinoid-sensitive and cannabinoid-insensitive basket cells. Nat Neurosci 9:807-815.

Goldberg EM, Jeong HY, Kruglikov I, Tremblay R, Lazarenko RM, Rudy B (2011) Rapid developmental maturation of neocortical FS cell intrinsic excitability. Cereb Cortex 21:666-682.

Grubb MS, Burrone J (2010) Activity-dependent relocation of the axon initial segment fine-tunes neuronal excitability. Nature 465:1070-1074.

Gulyás AI, Miles R, Hájos N, Freund TF (1993a) Precision and variability in postsynaptic target selection of inhibitory cells in the hippocampal CA3 region. Eur J Neurosci 5:1729-1751.

Gulyás AI, Miles R, Sík A, Tóth K, Tamamaki N, Freund TF (1993b) Hippocampal pyramidal cells excite inhibitory neurons through a single release site. Nature 366:683-687.

Gulyás AI, Szabó GG, Ulbert I, Holderith N, Monyer H, Erdélyi F, Szabó G, Freund TF, Hájos N (2010) Parvalbumin-containing fast-spiking basket cells generate the field potential oscillations induced by cholinergic receptor activation in the hippocampus. J Neurosci 30:15134-15145.

Hu H, Martina M, Jonas P (2010) Dendritic mechanisms underlying rapid synaptic activation of fast-spiking hippocampal interneurons. Science 327:52-58.

Jenkins SM, Bennett V (2001) Ankyrin-G coordinates assembly of the spectrin-based membrane skeleton, voltage-gated sodium channels, and L1 CAMs at Purkinje neuron initial segments. J Cell Biol 155:739-746.

Jonas P, Racca C, Sakmann B, Seeburg PH, Monyer H (1994) Differences in Ca2+ permeability of AMPA-type glutamate receptor channels in neocortical neurons caused by differential GluR-B subunit expression. Neuron 12:1281-1289.

Kaneko T, Fujiyama F (2002) Complementary distribution of vesicular glutamate transporters in the central nervous system. Neurosci Res 42:243-250.

Kawaguchi Y (1995) Physiological subgroups of nonpyramidal cells with specific morphological characteristics in layer II/III of rat frontal cortex. J Neurosci 15:2638-2655.

Kawaguchi Y, Kubota Y (1997) GABAergic cell subtypes and their synaptic connections in rat frontal cortex. Cereb Cortex 7:476-486.

Klausberger T, Magill PJ, Márton LF, Roberts JD, Cobden PM, Buzsáki G, Somogyi P (2003) Brain-state- and cell-type-specific firing of hippocampal interneurons in vivo. Nature 421:844-848.

Kuba H, Oichi Y, Ohmori H (2010) Presynaptic activity regulates Na+ channel distribution at the axon initial segment. Nature 465:1075-1078.

Li XG, Somogyi P, Tepper JM, Buzsáki G (1992) Axonal and dendritic arborization of an intracellularly labeled chandelier cell in the CA1 region of rat hippocampus. Exp Brain Res 90:519-525.

Lien CC, Jonas P (2003) Kv3 potassium conductance is necessary and kinetically optimized for high-frequency action potential generation in hippocampal interneurons. J Neurosci 23:2058-2068.

Massi L, Lagler M, Hartwich K, Borhegyi Z, Somogyi P, Klausberger T (2012) Temporal Dynamics of Parvalbumin-Expressing Axo-axonic and Basket Cells in the Rat Medial Prefrontal Cortex In Vivo. J Neurosci 32:16496-16502.

Meyer AH, Katona I, Blatow M, Rozov A, Monyer H (2002) In vivo labeling of parvalbumin-positive interneurons and analysis of electrical coupling in identified neurons. J Neurosci 22:7055-7064.

Miles R (1990) Synaptic excitation of inhibitory cells by single CA3 hippocampal pyramidal cells of the guinea-pig in vitro. J Physiol 428:61-77.

Miles R, Tóth K, Gulyás AI, Hájos N, Freund TF (1996) Differences between somatic and dendritic inhibition in the hippocampus. Neuron 16:815-823.

Nörenberg A, Hu H, Vida I, Bartos M, Jonas P (2010) Distinct nonuniform cable properties optimize rapid and efficient activation of fast-spiking GABAergic interneurons. Proc Natl Acad Sci U S A 107:894-899.

Pawelzik H, Hughes DI, Thomson AM (2002) Physiological and morphological diversity of immunocytochemically defined parvalbumin- and cholecystokinin-positive interneurones in CA1 of the adult rat hippocampus. J Comp Neurol 443:346-367.

Pouille F, Scanziani M (2001) Enforcement of temporal fidelity in pyramidal cells by somatic feed-forward inhibition. Science 293:1159-1163.

Richter K, Langnaese K, Kreutz MR, Olias G, Zhai R, Scheich H, Garner CC, Gundelfinger ED (1999) Presynaptic cytomatrix protein bassoon is localized at both excitatory and inhibitory synapses of rat brain. J Comp Neurol 408:437-448.

Sík A, Tamamaki N, Freund TF (1993) Complete axon arborization of a single CA3 pyramidal cell in the rat hippocampus, and its relationship with postsynaptic parvalbumin-containing interneurons. Eur J Neurosci 5:1719-1728.

Sohal VS, Zhang F, Yizhar O, Deisseroth K (2009) Parvalbumin neurons and gamma rhythms enhance cortical circuit performance. Nature 459:698-702.

tom Dieck S, Sanmarti-Vila L, Langnaese K, Richter K, Kindler S, Soyke A, Wex H, Smalla KH, Kampf U, Franzer JT, Stumm M, Garner CC, Gundelfinger ED (1998) Bassoon, a novel zinc-finger CAG/glutamine-repeat protein selectively localized at the active zone of presynaptic nerve terminals. J Cell Biol 142:499-509.

Tukker JJ, Fuentealba P, Hartwich K, Somogyi P, Klausberger T (2007) Cell type-specific tuning of hippocampal interneuron firing during gamma oscillations in vivo. J Neurosci 27:8184-8189.

Woodruff A, Xu Q, Anderson SA, Yuste R (2009) Depolarizing effect of neocortical chandelier neurons. Front Neural Circuits 3:15.

Woodruff AR, McGarry LM, Vogels TP, Inan M, Anderson SA, Yuste R (2011) State-dependent function of neocortical chandelier cells. J Neurosci 31:17872-17886.

Xu X, Callaway EM (2009) Laminar specificity of functional input to distinct types of inhibitory cortical neurons. J Neurosci 29:70-85.

Zemankovics R, Káli S, Paulsen O, Freund TF, Hájos N (2010) Differences in subthreshold resonance of hippocampal pyramidal cells and interneurons: the role of h-current and passive membrane characteristics. J Physiol 588:2109-2132.

Zhu Y, Zhu JJ (2004) Rapid arrival and integration of ascending sensory information in layer 1 nonpyramidal neurons and tuft dendrites of layer 5 pyramidal neurons of the neocortex. J Neurosci 24:1272-1279.

Acknowledgements: The authors are grateful to Dr. Szabolcs Káli for his help with the analysis, to Dr. Zoltán Nusser for providing the use of the FV 1000 Olympus confocal microscope, to Dr. Viktória Vereczki for her help with Neurolucida reconstructions, and to Erzsébet Gregori for her excellent technical assistance. The authors acknowledge helpful discussion with Drs Attila Gulyás and Szabolcs Kali. We also thank Dr. István Katona for the use of an electrophysiological setup at the beginning of this study, László Barna, the Nikon Microscopy Center at the Institute of Experimental Medicine, Nikon Austria GmbH, and Auro-Science Consulting, Ltd., for kindly providing microscopy support. The authors declare no conflict of interest.

Figure legends

Figure 1. The single-cell properties of axo-axonic cells and basket cells with fast spiking phenotype are distinct in the CA3 region of mouse hippocampus. Maximum intensity projection of confocal images of a representative axo-axonic cell (AAC, **A**) and a basket cell (BC, **B**) filled with biocytin. Borders of hippocampal layers are indicated with dashed lines. s.o., stratum oriens, s.p., stratum pyramidale, s.l., stratum lucidum, s.r., stratum radiatum, s.lm. stratum lacunosum-moleculare. Insets at top left corner show double immunofluorescent labeling for Ankyrin G (yellow) and biocytin (green). Arrows indicate biocytin-labeled boutons, arrowheads mark Ankyrin G-stained axon initial segments (AIS). AACs could be identified by rows of boutons forming close appositions with AISs, while boutons of BCs avoided them. Scale bars on the insets are 2.5 μm for the AAC and 10 μm for the BC.**C, D,** Voltage responses to hyperpolarizing (100 pA) or depolarizing (200 pA and 600 pA) current steps, in AACs (**C**) and BCs (**D**). Calibrations, 200 ms and 20 mV. **E,** Single-cell properties distinct in the two cell types. Here on the graphs and in Figures 2-7 each triangle represents a value from an individual cell, bars show the median of values in each group and asterisks indicate significant differences. Comparison of rheobase ($p=0.036$) action potential (AP) threshold ($p=0.0015$), AP half-width ($p=0.044$), input resistance ($p=0.019$) accommodation ratio ($p<0.001$) and spike frequency ($p=0.028$) are shown. Significance levels here and in all graphs: *: $p<0.05$, **: $p<0.01$, ***: $p<0.001$.

Figure 2. Determining the magnitude of excitatory synaptic inputs at spiking threshold in AACs and BCs. **A,** Family of responses obtained in a representative cell upon focal stimulation of fibers with increasing stimulus intensities in loose-patch, current-clamp or voltage-clamp mode. Rmp, resting membrane potential. **B,** Examples of discharging a cell in loose-patch and current-clamp mode. AP latencies (i.e. spike peak latency) detected extra- or intracellularly were calculated as the time between the beginning of the stimulus artifact and the AP peak. **C,** Comparison of the probability and the peak latency of spikes recorded extra- and intracellularly in the same cell in response to equivalent, gradually increasing stimulus intensities. Open squares show average values of six consecutive loose-patch measurements at each stimulus intensity, while filled gray

circles indicate corresponding current-clamp data. **D,** The amplitude of evoked EPSPs and EPSCs linearly increased as a function of stimulus intensity. From the EPSP/C amplitude vs. stimulus intensity curves we determined the size of EPSP/Cs and stimulus intensities needed to discharge the cells (7μA, outlined with square frames). **E,** Comparison of the amplitude of EPSPs (p=0.027) and EPSCs (p=0.257) at spike threshold in AACs and BCs. **F,** Lower stimulus intensities were needed to discharge BCs compared to AACs (p=0.001).

Figure 3. Kinetic properties of EPSCs evoked by focal stimulation of fibers in the stratum oriens in AACs and BCs are similar. **A,** Representative EPSCs at spike threshold in an AAC and a BC averaged from 6 consecutive traces. **B,** 20-80% rise time (p=0.780) and decay time constant (P=0.101) of evoked EPSCs in AACs and BCs were not different.

Figure 4. AMPA and NMDA receptor-mediated synaptic currents in AACs and BCs are comparable. **A,** EPSCs evoked by focal stimulation in a cell at different holding potentials in the absence or presence of 5 μM NBQX. Traces are averages of 6 consecutive sweeps. **B,** Rectification indices for AMPA receptor-mediated synaptic currents (p=0.424) and the fraction of NMDA receptor-mediated synaptic currents in the evoked synaptic responses (p=0.257) in AACs and BCs were similar.

Figure 5. Comparison of sEPSC properties. **A,** Representative sEPSC recordings obtained in AACs and BCs. **B,** Averages of 600 consecutive sEPSC events from the same recordings as in **A**. **C,** Peak amplitude (p=0.689), inter-event interval (p=0.013), 20-80% rise time (p=0.575) and decay time constant (p=0.171) of sEPSCs in AACs and BCs are plotted.

Figure 6. Excitatory synapse density on the proximal dendrites of AACs and BCs is similar. **A, D,** Triple immunofluorescent labeling for VGluT1 (blue), Bassoon (green) and biocytin (red). Scale bars are 6 μm. **B, C, E, F,** Contact sites on dendrites at higher magnification. Scale bars are

2 μm. Arrowheads indicate putative excitatory terminals expressing VGluT1 together with Bassoon labeling, which faces toward the labeled dendrites, indicating the presence of synaptic contacts. Stars mark VGluT1-immunonegative (putative inhibitory or subcortical) axon endings terminating on the labeled dendrites. **G,** Glutamatergic input density on the labeled dendrites in stratum oriens (p=0.377), strata pyramidale and lucidum (p=0.786), and stratum radiatum (p=0.092) obtained from 4 AACs and 4 BCs. Values derived from AACs are indicated in black, while those from BCs are gray. Here on the box charts and in Figure 7, the mean (small open square), the median (midline of the big box), the interquartile range (large box), and the 5/95% values (end of the whiskers) are shown.

Figure 7. Dendritic arborization of AACs and BCs are distinct. **A,** Maximal intensity projection confocal images of two AACs and two BCs and their dendrites reconstructed with Neurolucida software. **B,** Box chart comparison of soma surface (p=0.061), total dendritic length (p=0.004), and dendritic length in different hippocampal layers obtained from 15 AACs and 8 BCs (or, stratum oriens: p=0.010, rad, stratum radiatum: p=0.007). **C,** Comparison of the dendritic length, the number of dendrites and the number of nodes between the two PV-positive interneuron types as a function of dendritic order. **D,** Sholl Analysis of AACs and BCs. Left: a summary graph of the number of the intersections on the apical or basal dendrites as a function of radial distance from the soma; middle and right: the number of intersections on the apical or basal dendrites is shown separately as a function of distance from the soma.

Figure 8. Relationship between the sEPSC rate recorded in individual cells and the corresponding total dendritic length at different distances (50, 100, 150 and 350 μm) from the soma. Lines in graphs indicate significant correlations.

Table 1. Membrane properties of PV+ interneurons innervating the perisomatic region of pyramidal cells in the CA3 region of the hippocampus. Data are presented as the median with the first and third quartiles in parentheses. Significant differences ($p<0.05$) shown in bold were determined with the Mann-Whitney test.

	AAC	n	BC	n	p
Rheobase (pA)	**113 (80-188)**	**20**	**150 (150-275)**	**13**	**0.036**
AP threshold (mV)	**-33.3 (-37.7--31.95)**	**15**	**-38 (-41.6--36.3)**	**13**	**0.0015**
AHP ampl (mV)	19.95 (15.3-21.3)	15	19.6 (16.7-21.4)	13	0.765
AHP 25% decay (ms)	**10.65 (7.03-18.8)**	**20**	**5.8 (4.6-6.85)**	**13**	**0.019**
AHP 50% decay (ms)	**20.75 (14.03-40)**	**20**	**9.7 (7.75-11.2)**	**13**	**0.016**
AHP 75% decay (ms)	**30.15 (16.58-69.65)**	**20**	**13.5 (10.7-17.3)**	**13**	**0.020**
AP half-width (ms)	**0.45 (0.4-0.5)**	**20**	**0.35 (0.3-0.4)**	**13**	**0.044**
Spike frequency (Hz)	**138 (120-148)**	**20**	**166 (134-174)**	**13**	**0.028**
Accommodation ratio	**1.64 (1.58-2.00)**	**15**	**1.03 (0.99-1.11)**	**13**	**$1.2*10^{-5}$**
Ratio of AP amplitude adaptation	0.69 (0.52-0.8)	15	0.65 (0.62-0.73)	13	0.596
Resting membrane potential (mV)	-46.5 (-50--43)	36	-45 (-50--40)	24	0.154
Input resistance (MOhm)	**122.7 (86.5-175.6)**	**19**	**82.7 (67.1-111)**	**8**	**0.019**
Membrane time constant (ms)	13.71 (10.04-16.38)	15	13.15 (10.71-14.13)	13	0.674
Membrane capacitance (pF)	103.9 (72.7-148.7)	15	151.4 (86-204.4)	13	0.322
Relative sag amplitude	0.227 (0.130-0.258)	15	0.280 (0.091-0.336)	13	0.512

Table 2. Properties of excitatory synaptic input recorded in AACs and BCs. Data are presented as the median with the first and third quartiles in parentheses. Significant differences ($p<0.05$) shown in bold were determined with the Mann-Whitney test.

	AAC	n	BC	n	p
Amplitude of threshold eEPSP (mV)	**6 (5.21-7.6)**	**13**	**4.58 (3.74-4.64)**	**7**	**0.027**
Amplitude of threshold eEPSC (pA)	199 (149-312)	11	255 (186-402)	7	0.257
Amplitude of maximal eEPSC (pA)	350 (205-800)	27	475 (360-650)	18	0.701
Stimulus intensity at AP threshold (μA)	**18 (15-32.5)**	**16**	**9 (7-11)**	**10**	**0.001**
20-80 % rise time of eEPSC (ms)	0.54 (0.44-0.61)	19	0.53 (0.4-0.7)	11	0.780
Decay time constant of eEPSC (ms)	3.06 (2.43-4.47)	14	2.38 (1.46-3.07)	10	0.101
Rectification index of AMPA R-med. currents	0.195 (0.1-0.3)	18	0.105 (0.01-0.35)	6	0.424
Fraction of NMDA R-med. currents	0.105 (0.067-0.2)	18	0.215 (0.086-0.49)	6	0.257
Peak amplitude of sEPSC (pA)	23.61 (19.34-28.03)	6	27.65 (19.88-30.85)	6	0.689
Interevent interval of sEPSC (ms)	**0.056 (0.038-0.134)**	**6**	**0.023 (0.016-0.030)**	**6**	**0.013**
20-80 % rise time of sEPSC (ms)	0.347 (0.253-0.447)	6	0.369 (0.353-0.374)	6	0.575
Decay time constant of sEPSC (ms)	1.83 (1.67-2.14)	6	2.07 (1.99-2.34)	6	0.171

Table 3. Morphological analysis of AACs and BCs. Data are presented as the median with the first and third quartiles in parentheses. Significant differences ($p<0.05$) shown in bold were determined with the Mann-Whitney test.

	AAC	n	BC	n	p
Length of Ank. G-stained segments (µm)	29.05 (22.45-38.75)	8	28.45 (24.6-33.3)	6	0.746
Dist. of Ank. G-stained segments from soma (µm)	4.35 (3.35-11.3)	8	6.8 (2.8-9.8)	6	1
# of inputs/50 μm^2 in str. oriens	15.40 (11.01-24.59)	9	21.95 (15.77-28.19)	6	0.377
# of inputs/50 μm^2 at prox. region	12.44 (6.51-18.76)	10	15.80 (12.78-17.47)	6	0.786
# of inputs/50 μm^2 in str. radiatum	15.66 (8.45-19.99)	11	19.92 (18.99-27.9)	5	0.257
Surface of soma (μm^2)	2329 (1957-2940)	9	3428 (2686-4990)	8	0.061
Total dendritic length (µm)	**3325 (2743-3614)**	**15**	**4978 (3656-5480)**	**8**	**0.004**
Dendritic length in str. oriens(µm)	**570 (0.1-1222)**	**15**	**1493 (1025-2358)**	**8**	**0.010**
Dendritic length in str. pyr. (µm)	480 (333-541)	15	565 (455-675)	8	0.186
Dendritic length in str. luc. (µm)	179 (97-374)	15	132 (78-219)	8	0.420
Dendritic length in str. rad. (µm)	**1259 (805-1571)**	**15**	**1877 (1563-2363)**	**8**	**0.007**
Dendritic length in str. lm. (µm)	337 (40-1259)	15	292 (113-581)	8	0.457
Dendritic length at 3rd order (µm)	**587 (448-896)**	**15**	**1271 (764-1561)**	**8**	**0.006**
Dendritic length at 4th order (µm)	601 (405-920)	14	895 (810-995)	8	0.094
Dendritic length at 5th order(µm)	**376 (179-649)**	**14**	**829 (546-1171)**	**8**	**0.013**

# of dendrites at 3rd order	**8 (6-10)**	**15**	**14 (9.75-14.75)**	**8**	**0.017**
# of dendrites at 4th order	**8 (4-10)**	**14**	**10 (8.5-13.5)**	**8**	**0.047**
# of dendrites at 5th order	**6 (4-8)**	**14**	**11 (8.5-13.5)**	**8**	**0.004**
# of nodes at 2nd order	**4 (3-5)**	**15**	**7 (4.5-7)**	**8**	**0.027**
# of nodes at 3rd order	4 (2-5)	14	5 (4.25-6.75)	8	0.051
# of nodes at 4th order	**3 (2-4)**	**14**	**5.5 (4.25-6.75)**	**8**	**0.004**
The highest order of dendr. segments	7 (6-9)	15	7.5 (7-8.75)	8	0.575
# of apical inters. at 150 µm	**2 (1.75-3.25)**	**14**	**4.5 (3-7.25)**	**8**	**0.020**
# of apical inters. at 200 µm	**2.5 (2-4.25)**	**14**	**6 (3.25-7.75)**	**8**	**0.033**
# of basal inters. at 50 µm	**3.5 (3-4.25)**	**14**	**6.5 (5-7.75)**	**8**	**0.009**
# of basal inters. at 100 µm	**4 (3-5)**	**14**	**8.5 (6.25-10.75)**	**8**	**0.003**
# of basal inters. at 150 µm	**3 (1.5-5.5)**	**13**	**7 (5.5-10.25)**	**8**	**0.004**
convex hull volume (μm^3)	$1.24*10^7$ (10^7-$1.8*10^7$)	15	$2.11*10^7$ ($1.33*10^7$-$2.67*10^7$)	8	0.165
Ratio of apical intersections, 300/150 µm	**2 (1.46-3)**	**14**	**0.95 (0.51-2.06)**	**10**	**0.049**
Ratio of apical intersections, 350/150 µm	**2.5 (1.19-3.75)**	**14**	**0.5 (0.16-1.83)**	**9**	**0.025**
Ratio of apical intersections, 300/200 µm	**1.73 (1.4-2)**	**14**	**0.94 (0.45-1.5)**	**10**	**0.021**
Ratio of apical intersections, 350/200 µm	**1.93 (0.79-3.13)**	**14**	**0.33 (0.15-1.21)**	**9**	**0.037**

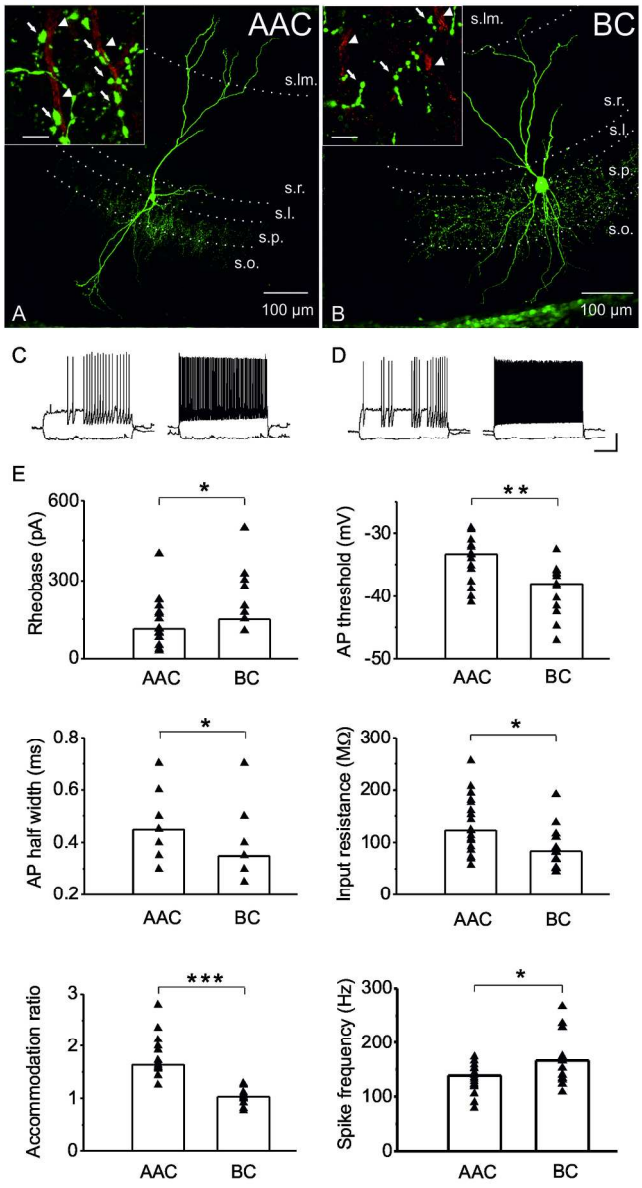

163x275mm (300 x 300 DPI)

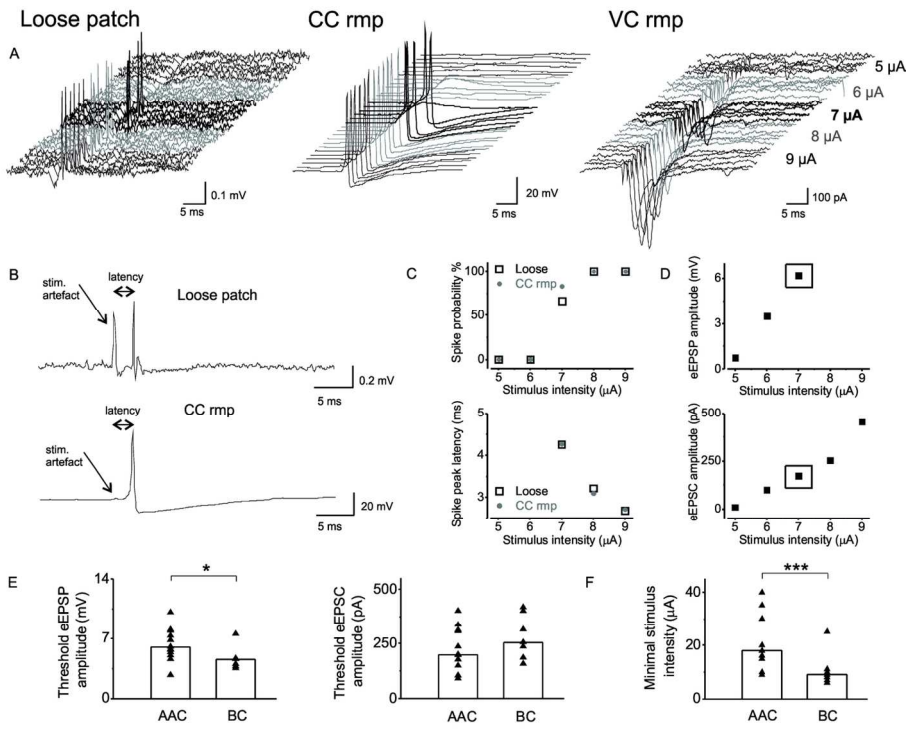

141x103mm (300 x 300 DPI)

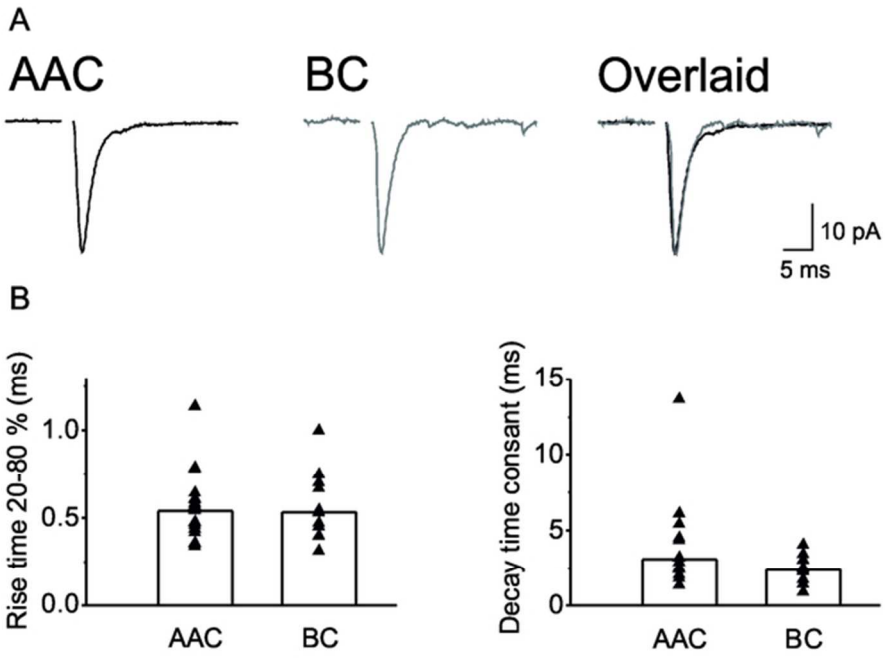

60x39mm (300 x 300 DPI)

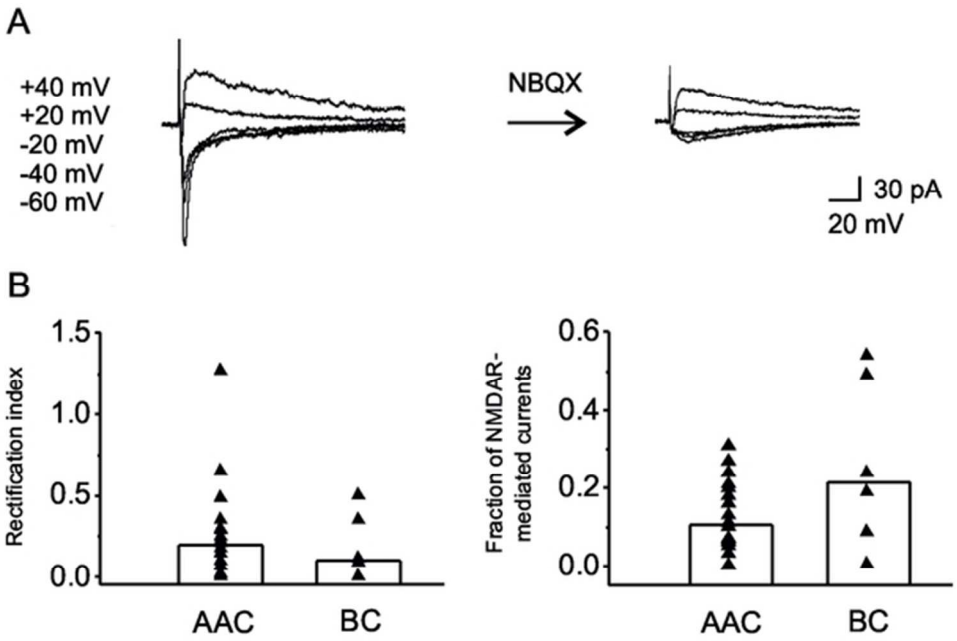

53x35mm (300 x 300 DPI)

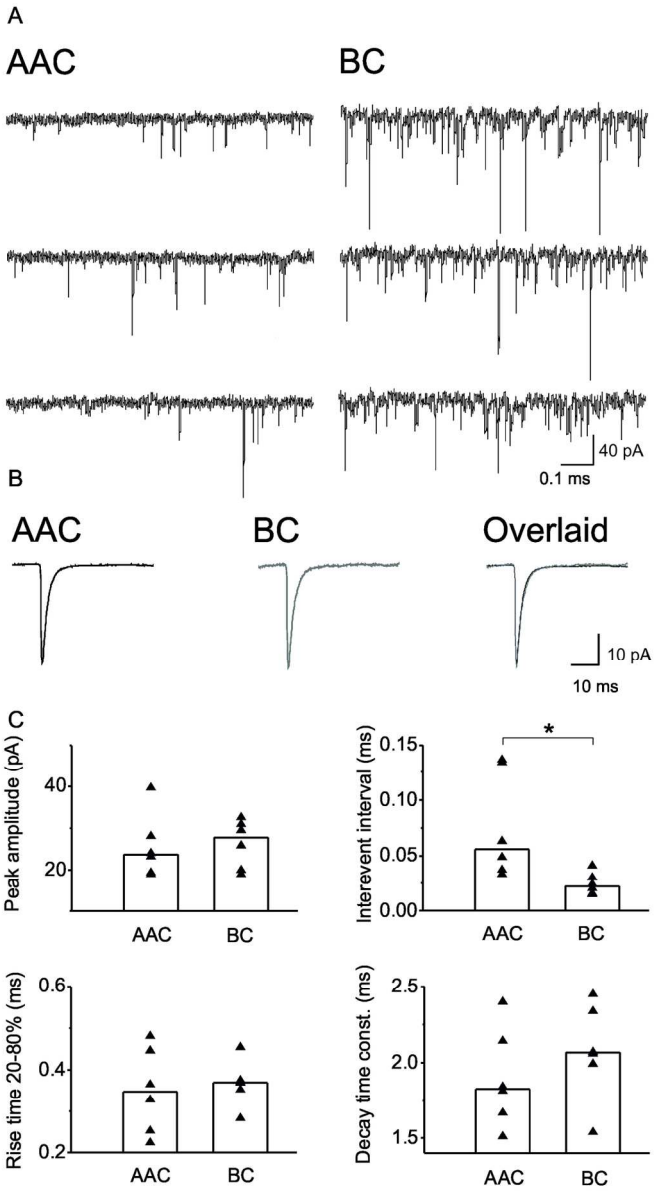

150x192mm (300 x 300 DPI)

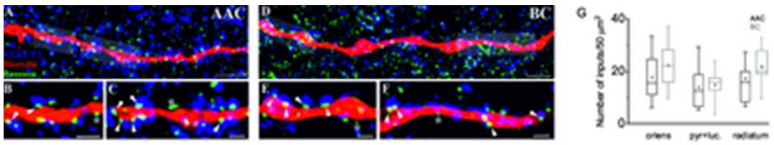

33x6mm (300 x 300 DPI)

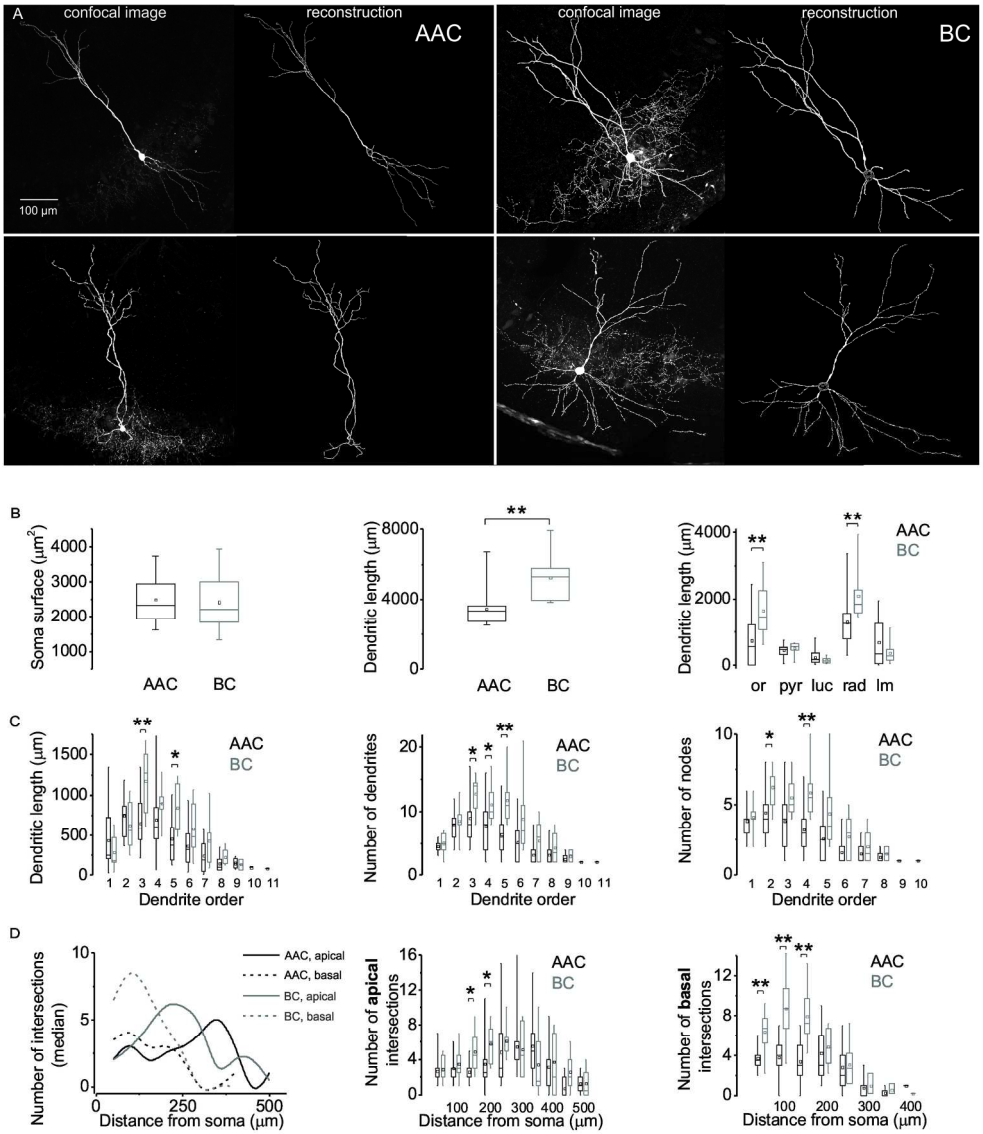

212x243mm (300 x 300 DPI)

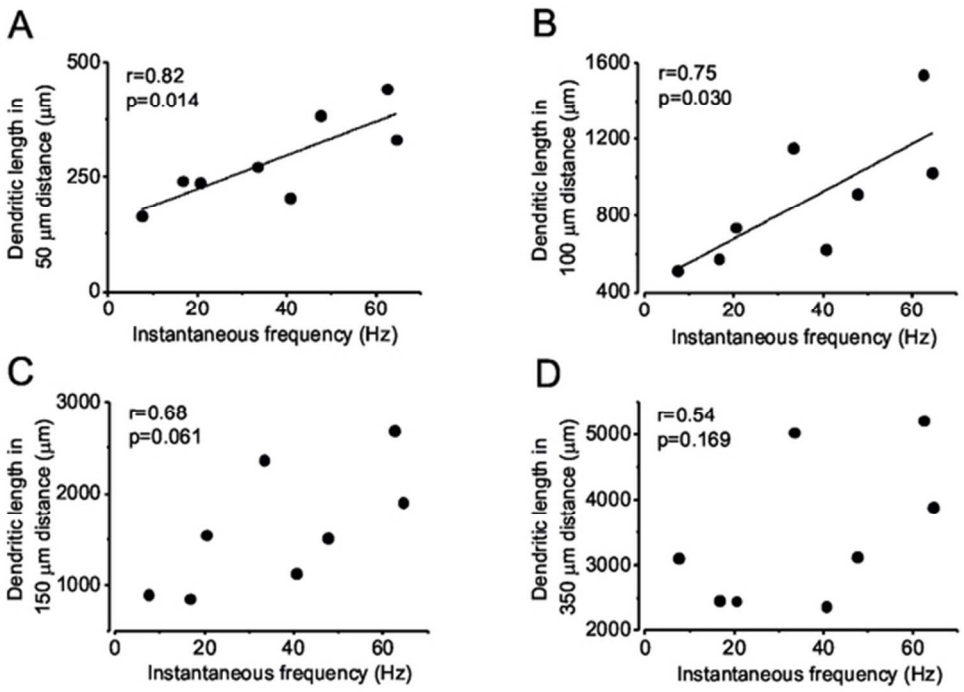

53x38mm (300 x 300 DPI)